Int J Earth Sci (Geol Rundsch) (2017) 106:531–548
DOI 10.1007/s00531-016-1370-8

ORIGINAL PAPER

Very low-temperature metamorphism in Ordovician metasedimentary rocks above and below the Sardic unconformity, SW Sardinia, Italy

M. Franceschelli[1] · S. Battaglia[2] · G. Cruciani[1] · S. Pasci[3] · M. Puxeddu[2]

Received: 11 January 2016 / Accepted: 30 June 2016 / Published online: 15 July 2016

Abstract In the Iglesiente region, the Cabitza and Monte Argentu Formations are separated by an angular unconformity known as the Sardic unconformity. This is related to an early Ordovician mild compressional phase, known as the "Sardic phase". The pelitic samples from the structurally lower Cabitza Formation consist of alternating reddish phyllosilicate-rich and whitish phyllosilicate-poor, sialic layers, whose S_0 bedding plane is parallel to a pre-Variscan S_{1P} schistosity overprinted by the Variscan S_{1V} schistosity. Pelitic samples from the Monte Argentu Formation are characterized by a Variscan S_{1V} axial plane schistosity. Samples from the two formations consist of quartz and phyllosilicates. The latter are potassic white mica, chlorite, paragonite, locally kaolinite, and pyrophyllite. The illite crystallinity values determined for the Cabitza samples are 0.25–0.31, with an average of 0.29; meanwhile, the Monte Argentu samples produce values of 0.33–0.38, with an average of 0.35. The chlorite crystallinity and b_0 of potassic white mica values show greater heterogeneity in the Cabitza than the Monte Argentu samples. The b_0 values and P–T pseudosections allow us to confirm that there is no significant difference in the P–T metamorphism conditions between the Cabitza and Monte Argentu samples. The Iglesiente region, which is considered to be the rift zone behind the Middle Ordovician Sarcidano–Barbagia volcanic arc, underwent the "Sardic phase", giving rise to E–W folds. These were first overprinted by weak E–W, and then by stronger N–S-oriented Variscan deformation events.

Keywords Low-temperature metamorphism · Phyllosilicate · Sardic phase · Iglesiente · Variscan Sardinia

Introduction

In SW Sardinia (Iglesiente), along the Gonnesa–Nebida road, a spectacular angular unconformity between an underlying Lower Cambrian–Ordovician sequence and overlying transgressive Ordovician conglomerates ("Puddinga" Auct.) has attracted the attention of various geologists since the start of the 1930s. Later, this unconformity was considered to be witness to a major pre-Variscan tectonic event named by Stille (1939) as the "Sardic Phase". This Ordovician event generated E–W trending open folds. Unfortunately, the first Variscan phase gave rise to mild E–W folds that strengthened the E–W pre-Variscan folds, creating ambiguities and problems of interpretation that led some authors to deny the existence of the Sardic Phase (Del Bono 1965; Brower 1987; Lüneburg and Lebit 1998).

The literature has mainly been concerned with distinguishing the structural features of the Sardic and Variscan deformation phases. Little attention has been paid to the potential contribution of petrographic, mineralogical and geochemical studies in finding a solution to the ambiguities and unsolved problems of interpretation deriving from the overlapping Sardic and Variscan folds with the same E–W orientation. The goal of this paper is to use field geology,

✉ G. Cruciani
gcrucian@unica.it

[1] Dipartimento di Scienze Chimiche e Geologiche, Università di Cagliari, Via Trentino 51, 09127 Cagliari, Italy

[2] Istituto di Geoscienze e Georisorse, CNR Pisa, Via Moruzzi 1, 56124 Pisa, Italy

[3] Via Mar Egeo n. 29, 09045 Quartu S. Elena, Italy

mineral chemistry, X-ray diffraction (XRD), illite and chlorite crystallinity, the b_0 of potassic white mica, and geothermobarometry to make a contribution to what is known of the low-temperature metamorphism in the pelitic rocks above and below the Sardic unconformity. Additionally, the occurrence of a low-temperature metamorphism that accompanied the Ordovician Sardic phase is verified, while some light is shed on the nature and geological significance of this tectonic phase.

Geological framework

The metamorphic basement of Iglesiente–Sulcis (Fig. 1a, b) belongs to the External Zone, which is the southernmost segment of the Variscan chain in Sardinia. Moving northwards, the other segments are the External Nappe Zone, the Internal Nappe Zone and the Inner Zone, which are composed of medium- to high-grade metamorphic rocks (Franceschelli et al. 1982), including several types of migmatite (Carmignani et al. 2001; Cruciani et al. 2001, 2014a, b; Massonne et al. 2013) and metabasite lenses with eclogite and granulite facies relics (Franceschelli et al. 2002; Cruciani et al. 2012).

Detailed information on the Sulcis and Iglesiente Palaeozoic sequence can be found in Leone et al. (1991, 2009), Pillola and Gross (1982) and Pillola et al. (1995, 2008).

In the Iglesiente–Sulcis, the pre-Sardic succession includes, from the bottom to the top, the following: the Nebida, Gonnesa, Campo Pisano and Cabitza Formations (Fms.) which range in age from the Lower Cambrian to the

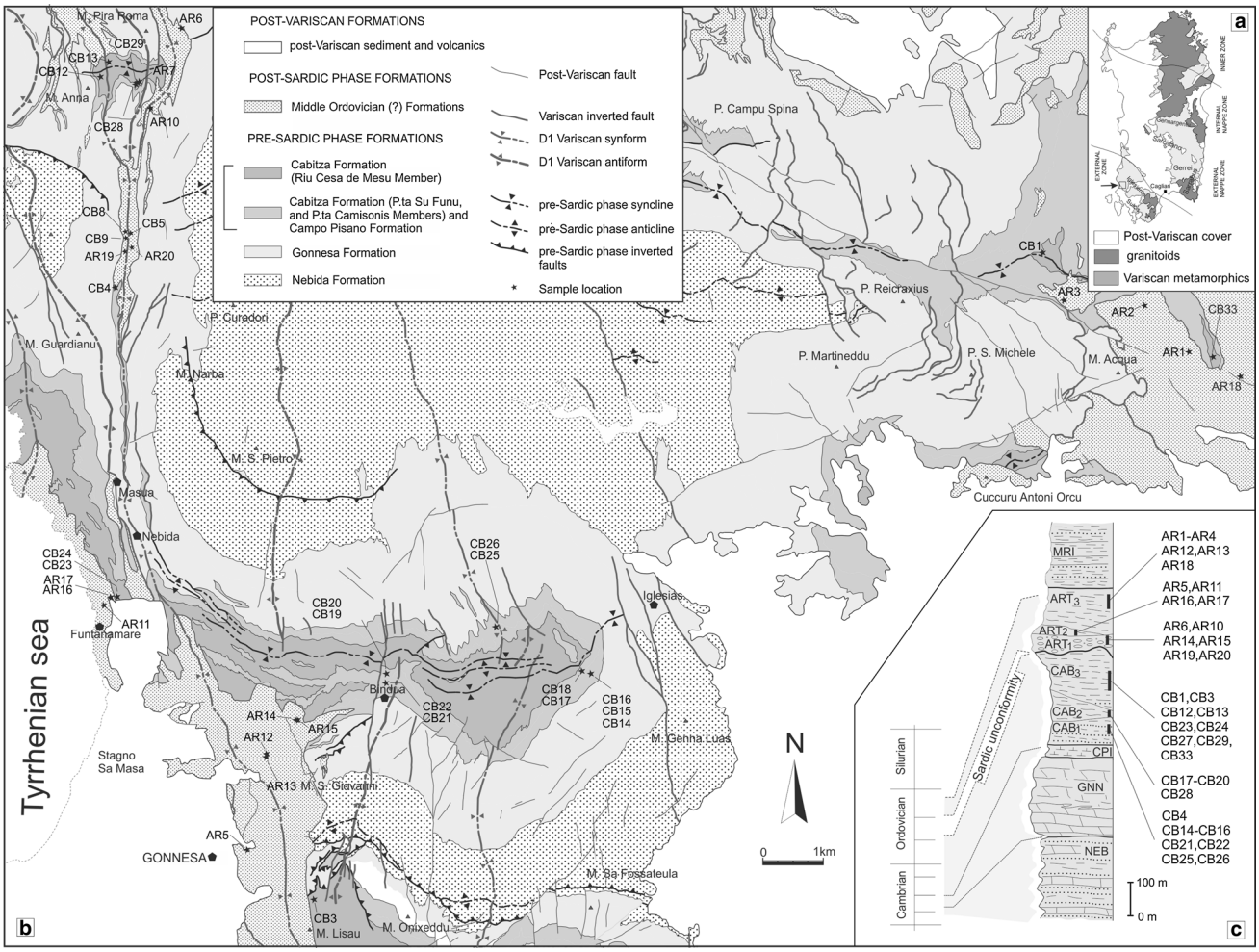

Fig. 1 **a** Tectonic sketch map of the Variscan basement of Sardinia (modified from Carmignani et al. 2001); **b** geological sketch map of the Gonnesa area, including the key localities of the Sardic unconformity. The studied samples are reported as CB for samples from the formations underlying the Sardic unconformity and as AR samples for those from formations overlying it (modified from Pasci et al. in press); and **c** lithostratigraphic reconstruction of the formations underlying and overlying the Sardic unconformity. In the CBF, three members have been distinguished: CAB1, CAB2, and CAB3 (see text). In the MAF, three members have also been identified (ART1, ART2 and ART3). *Symbols*: Nebida Fm (NEB), Gonnesa Fm (GNN), Campo Pisano Fm (CPI) and Monte Orri Fm (MRI)

Lower Arenig (Fig. 1c). The post-Sardic succession is composed, from the bottom to the top, by the Monte Argentu Fm. up to the Pala Manna Complex, with an age span from the Middle Arenig to the Carboniferous. The samples studied are from the Cabitza and Monte Argentu Fms, which are located immediately below and above the Sardic unconformity, respectively.

The Cabitza Formation

The Cabitza Formation (CBF) largely outcrops in the Iglesiente region and is the most recent formation of the pre-Sardic sedimentary sequence. From the bottom to the top, the following three members have been distinguished by Pasci et al. (in press): Punta Camisonis, Punta Su Funu and Riu Cea de Mesu. The Punta Camisonis member consists of metasiltites, slates and metasandstones with still recognizable sedimentary structures (CAB1, Fig. 1c). The Punta Su Funu member is represented by alternating red and green metasiltites and slates (CAB2, Fig. 1c). The Riu Cea de Mesu member forms a monotonous sequence of alternating dark green to grey metapelites and rare, thin, laminated metasiltite layers. The base of this member is characterized by the occurrence of decimetre-thick metasandstone layers (CAB3, Fig. 1c). The geochronological attribution of the Sardic Phase can be restricted to the Middle Arenig–Caradoc (Tremadocian, and maybe Floian, Sandbian, ISC) interval on the basis of: the discovery of Upper Tremadocian–Lower Arenig fossils by Pillola et al. (2008) within this uppermost member of the CBF, and the well-known Caradocian (Sandbian, ISC) age of the first fossil faunas found in the post-Sardic Fms (Carmignani et al. 2001 and references therein).

The Monte Argentu Formation

The Monte Argentu Formation (MAF) consists at the base of coarse to very coarse clastic continental syntectonic deposits (Martini et al. 1991) which grade upwards into finer sediment (mainly metasiltites). Three members have been distinguished from the bottom to the top: Punta sa Broccia: polygenic metaconglomerates, metabreccias, metasandstones and metasiltites (ART1, Fig. 1c); Rio is Arrus: grey metasiltites and metapelites (ART2, Fig. 1c); and Medau Murtas: reddish to greenish metasiltites and metapelites with minor metasandstones (ART3, Fig. 1c). The age of the entire formation, owing to the paucity of fossils, may be placed between the Tremadocian–Lower Arenig (Tremadocian and maybe Floian, ISC) age of the uppermost member of the CBF and the Caradoc (Sandbian, ISC) age of the first dated overlying sediment (Leone et al. 1991, 2009).

Pre-Variscan and Variscan tectonics of the Iglesiente region

The complex interpretation of the structural framework of the Iglesiente region has led most authors to identify four deformation phases, the first of which is considered to be Ordovician in age ("Sardic phase") and the following of Variscan age (Arthaud 1963, 1970; Poll and Zwart 1964; Poll 1966; Dunnet 1969; Carmignani et al. 1982, 1986, 2001; Carosi et al. 1992).

The Sardic phase (Stille 1939) is witnessed by E–W trending open folds. The age is indicated by the Sardic unconformity (Teichmüller 1931), which is an angular unconformity separating the underlying Cambrian–Lower Arenig sequence from the overlying Middle Arenig–Upper Ordovician transgressive metaconglomerates (Fig. 2a). Recent field work and mapping (Pasci et al. in press) have improved the stratigraphy of the Cambrian–Ordovician sequences defined by Pillola (1991) and Leone et al. (1991), allowing for a better definition of the structural frame. All these studies have allowed the reverse faults, overthrusts and km-sized folds observed in the Cambrian–Lower Ordovician sequence to be attributed to a tectonic phase that is active between the Lower Ordovician and the Middle–Upper Ordovician. These structures survived and are still recognizable despite a significant Variscan overprint (Fig. 2b–d). Evidence of a pre-Variscan deformation phase has been recognized on the basis of geological mapping (Fig. 1b) in some key areas.

Near Gonnesa, the MAF unconformably covers previous overthrusts, reverse faults and km-sized folds affecting the underlying Cambro-Ordovician sequence (Fig. 1b). As a general feature in the CBF, the sedimentary layering is parallel to a pre-Variscan S_{1P} schistosity that never appears as an axial plane foliation (Fig. 2c). Both the sedimentary layering and pre-Variscan S_{1P} schistosity are cut by an almost orthogonal Variscan S_{1V} schistosity that is clearly observable in the overlying MAF (Fig. 2c). On the coast of the village of Masua, Variscan folds with N–S trending axes bend older pre-Variscan folds with E–W trending axes (Fig. 2e, f). In the same region, the older Gonnesa Fm. overthrusts the younger CBF. The superposition of deformation events from Ordovician (pre-Variscan) to late Variscan times gave rise to complex structural interferences. On a km-sized scale, Variscan folds with a vertical axial plane and N–S trending axes significantly deform the pre-Variscan folds with a vertical axial plane and E–W trending axes, producing domes and basins interference patterns.

The first Variscan phase produced gentle, discontinuous E–W trending folds (Fig. 2d) that tighten the previous structures and generate a very weak slaty cleavage. Despite

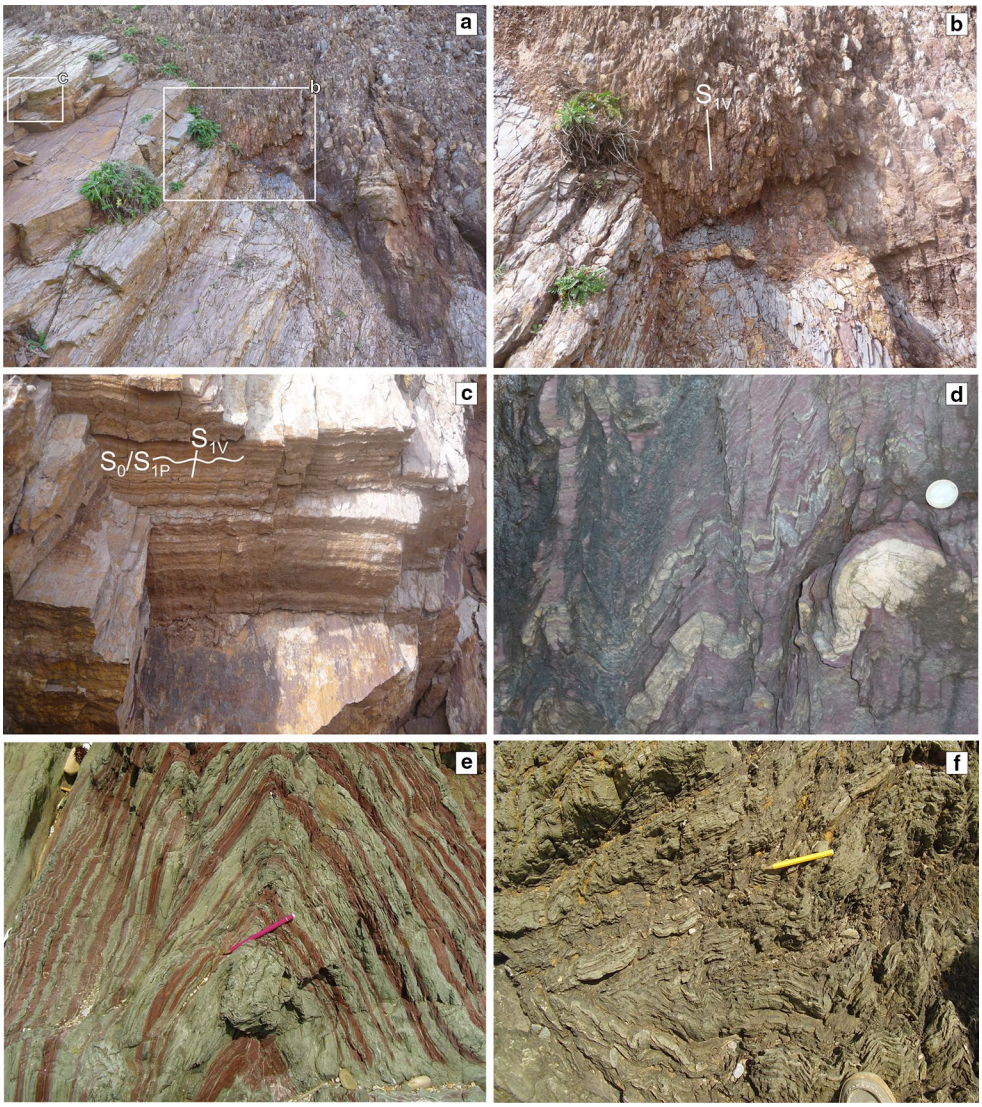

Fig. 2 **a** Sardic unconformity between the CBF (*left*) and the metaconglomerate of the MAF (*right*) along the coast road to Nebida; **b** detailed view of the two lithologies in contact at the unconformity; the S_{1V} foliation is also shown; **c** S_{1V} crenulation cleavage overprinting a previous S_0/S_{1P} schistosity in the metasiltites of CBF; **d** compositional layering in the MAF deformed by E–W striking folds and crenulation cleavage; **e** folds with an E–W-oriented subvertical axis in the metasiltite of the CBF near to Masua beach; **f** interference between the folds with an E–W-oriented *subvertical axis* (parallel to the pencil) and the N–S-oriented folds (orthogonal to pencil) on the quaternary marine abrasion surface near to Masua beach

their similar orientation, the Variscan deformations of this first phase are remarkably weaker than the pre-Variscan ones: their folds are more open, more discontinuous and less extended (compare Fig. 2d with Fig. 2e). The second Variscan phase, to which the main deformation is related, generated N–S trending folds, faults and overthrusts. A pervasive cleavage is commonly associated with the N–S folds, which have steep axial planes and W-directed vergence. The axial planar cleavage, which is always evident, shows a decreasing intensity from marly and pelitic lithotypes to sandstones and quartzites. W-vergent, steeply ENE dipping reverse faults, which are generally associated with broad cataclastic bands and E-vergent back-thrusts represent the late evolution of this deformative phase. These km-sized faults developed along the reversed limb of the main N–S trending folds. The third Variscan phase is characterized by minor structures with variable axial directions.

Analytical methods

Forty rock samples were collected as a whole from the MAF and CBF. Fresh unweathered rock samples were disaggregated under standard conditions with a jaw crusher

and then gently crushed in a mortar mill for ~3 min. The XRD patterns were recorded using a Philips PW1710 automatic diffractometer equipped with a long fine-focus Cu tube at the following instrumental settings: CuK_{α} Ni-filtered radiation; 40 kV; 20 mA; slits: ½° divergence and scatter, 0.2 mm receiving; continuous scanning; scan speed: 0.25°2θ per minute; and time constant: 4 s. The illite crystallinity index (IC) 10 Å peak and the chlorite crystallinity index 7 Å peak were done via a computer on fitted peaks using Krumm's (1996) WINFIT program, which determines the peak's full width at half maximum (FWHM) by first subtracting the background from the raw data and then operating the peak fitting through an asymmetrical Pearson VII function by retaining the $K_{\alpha 2}$ wavelength. All the measured illite and chlorite indices were calibrated with respect to the standard rock slab series provided by Kübler (1990, samples 32, 34 and 35) following the procedure reported in Leoni (2001). The b_0 parameter of potassic white mica was estimated on rock slates that are cut perpendicular to the schistosity (Sassi and Scolari 1974). The b_0 parameter was measured by step scanning the range of 58–64°2θ at ~0.27°2θ/min. XRF spectrometry on the bulk rock samples was used to determine the concentrations of the major elements according to the method by Franzini et al. (1975). Volatile components (H_2O and CO_2) were collectively determined as a loss on ignition (LOI) at 950 °C on powders dried at 110 °C. The FeO was determined by colorimetric titration. The microstructural study and BSE imaging were performed with a FEI Quanta 200 SEM equipped with an EDAX energy-dispersive spectroscopy (EDS) detector at the Centro Grandi Strumenti of Cagliari University. The chemical composition of the minerals was determined with a fully automated JEOL 8200 Super Probe at the Dipartimento di Scienze della Terra, University of Milano. The analytical conditions were those described in Cruciani et al. (2015a). The transmission electron microscopy (TEM) analyses were performed at Siena University using a JEOL 2010 TEM working at 200 kV, with a point resolution of 1.9 Å, following the methods described in Viti (2011).

Petrographical features

The CBF samples show alternations of rusty red and whitish millimetric layers (Fig. 3a). The former is characterized by an extreme abundance of opaque Fe oxides and moderate clast contents such as quartz and potassic white mica. In contrast, the whitish layers contain very fine-grained phyllosilicate, mostly illite, with several clasts of quartz and potassic white mica and opaque mineral trails (mostly Ti oxide and Fe oxide). In many samples, a faint schistosity is outlined by Fe–Ti oxides. Several clasts of detrital potassic white mica, quartz, chlorite and minor lithic fragments also occur. In one sample, very abundant rounded to polygonal opaque grains of haematite were observed. Of particular interest are some samples with a whitish layer that is some millimetres thick, very rich in clasts of quartz and potassic white mica, and sharply bounded by brownish layers containing abundant Fe–Ti oxides and lower amounts of potassic white mica and quartz clasts. The boundaries between these different layers mark the S_0 bedding plane that is parallel to a weak pre-Variscan S_{1P} schistosity, both of which are cut by the S_{1V} Variscan schistosity. The S_1v in the samples studied is not associated with mineral growth (Fig. 3a).

The samples of the MAF are characterized by a microcrystalline matrix, which surround several grains of detrital potassic white mica and quartz. Remarkable is the abundance of Fe oxides that explains the rusty red colour of these rock samples. Several samples from the MAF show the surface S_0 that is defined by the alternation between rusty red and whitish sedimentary layers and a well-defined S_{1V} surface crenulated by an S_{2V} schistosity, as revealed by strongly undulate strings of Fe and Ti oxides (Fig. 3b). In other samples, the S_{2V} schistosity is more pervasive, partially overprinting the S_{1V} schistosity. Investigations with an SEM revealed in the Monte Argentu samples the occurrence of zoned potassic white mica crystals (Fig. 3c) with a celadonite-rich core and a celadonite-poor rim, as well as many types of fine-grained phyllosilicate intergrowths such as chlorite/pyrophyllite, potassic white mica/pyrophyllite (Fig. 3d), chlorite/potassic white mica (Fig. 3e) and chlorite/paragonite (Fig. 3f), which are similar to those described by Franceschelli et al. (1989, 1998) in the low-grade metasediment of the Northern Apennines. The phyllosilicate assemblage of the studied samples is reported in Table 1. Minor differences were observed between the samples from the CBF and MAF. The mineral assemblages in both groups always include quartz, illite and chlorite (trioctahedral, di-trioctahedral), with an occurrence of paragonite in about 50 % of the CBF and 75 % of the MAF samples. Kaolinite, which was frequently observed in the CBF samples (35 % of samples), was found in only two samples from the MAF. Pyrophyllite occurs in 4 of 17 samples from the MAF and only two from the CBF. Mixed-layer components were observed in only two CBF samples. In some samples, the small peaks in intensity at $d = 4.94$ and 3.26 Å are probably due to the mixed-layer paragonite/potassic white mica described by Frey (1969). Other minerals detected in both the CBF and MAF include albite, Fe and Ti oxide, apatite, zircon, monazite, baryte and calcite.

Bulk chemical composition

The most pelitic layers within the two formations studied were sampled. Analyses of the major elements (wt%),

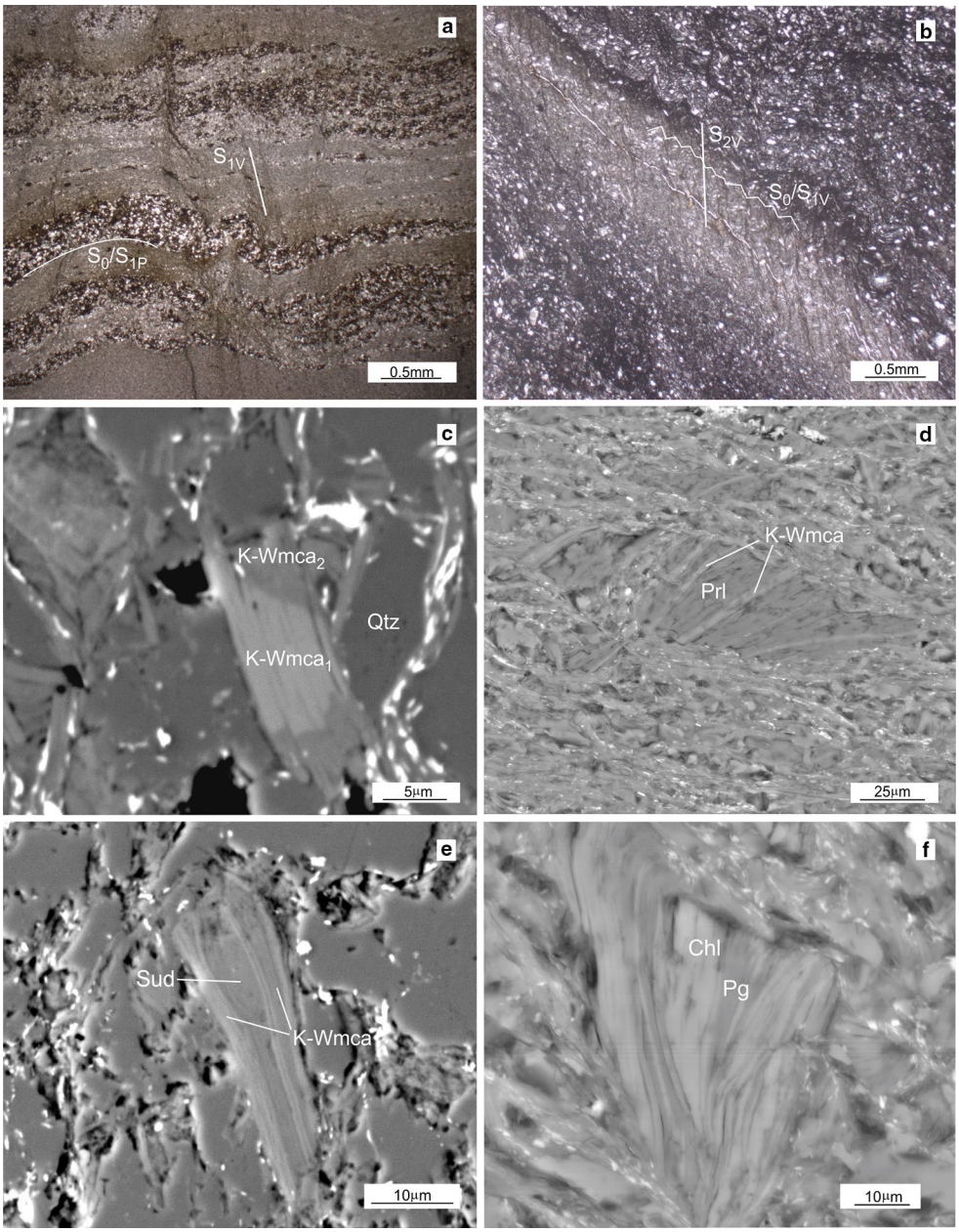

Fig. 3 **a** Photomicrograph of the CBF samples showing alternation of Fe oxide, quartz and phyllosilicate layers and phyllosilicate-rich layers. The S_0 bedding and pre-Variscan S_{1P} foliation are weakly crenulated by the S_{1V}. One polar; **b** photomicrograph of the MAF group samples showing the S_0/S_{1V} crenulated by the S_{2V}. One polar. SEM images of the MAF group samples; **c** zoned potassic white mica crystal with a celadonite-rich core (K-Wmca$_1$) and a celadonite-poor discontinuous rim (K-Wmca$_2$); **d** potassic white mica/pyrophyllite interleaving in a matrix made up of phyllosilicates; **e** interleaving of potassic white mica/Zn sudoite; and **f** interleaving chlorite/paragonite

together with Ba, Rb and Sr (ppm) of some selected samples, are reported in Table 2. The FeO in four samples was determined by colorimetric titration. The samples are characterized by a high Al_2O_3 content that is generally higher than 20 % and a low SiO_2 content that is mostly lower than 60 %.

In the K_2O/Na_2O vs. SiO_2/Al_2O_3 diagram (Wimmenauer 1984, not shown), all the samples plot in the pelite field. A comparison of the major element content between the CBF and MAF samples reveals no significant differences. The high K_2O contents in the range 3–6 wt% and the low Na_2O content below 1 wt% indicate a prevalence of K-bearing minerals such as illite, pyrophyllite, potassic white mica and K-feldspar over the Na-bearing minerals, i.e. paragonite and plagioclase.

Table 1 Mineral assemblages of 23 samples (CB) from the CBF and 17 samples (AR) from the MAF determined in the >2 μm fraction

Samples	K-Wmca	Chl	Prl	Pg	Pg/K-Wmca	Kao
CB1	x	x		x		
CB2	x	x		x		
CB3	x	x		x		
CB4	x	x		?		x
CB12	x	x				x
CB13	x	x				x
CB14	x	x			x	
CB15	x	x				
CB16	x	x				
CB17	x	x				
CB18	x	x			x	
CB19	x	x		x		
CB20	x	x				
CB21	x	x		x		x
CB22	x	x		x		x
CB23	x	x		x		
CB24	x	x				x
CB25	x	x				
CB26	x	x				
CB27	x	x		x?		
CB28	x	x	x			x
CB29	x	tr.	x	x?		x
CB33	x	x		x		
AR1	x	x		x		
AR2	x	x		x		
AR3	x	x				
AR4	x	x		x		
AR5	x	x		x		
AR6	x					
AR10	x		x	x		
AR11	x	x	x			
AR12	x	x				
AR13	x	x		x		x
AR14	x	x	x	x		
AR15	x	x	x	x		
AR16	x	x				
AR17	x	x?				
AR18	x	x		x		
AR19	x	x		x		
AR20	x	x		x		x

All the mineral assemblages include quartz. The mineral abbreviations according to Fettes and Desmons (2007)

K-Wmca potassic white mica

Phyllosilicate composition

Selected microprobe analyses of potassic white mica and chlorite from the CBF and MAF samples are set out in Tables 3 and 4. The structural formulas for potassic white mica were calculated using the CalcMin program (Brandelik 2009) with 42−(Ca + Ba) valencies, while those of chlorite were calculated on the basis of 14 oxygen equivalents. We encountered many problems in analysing the phyllosilicates from the fine-grained matrix and intergrowths. Often, the size

Table 2 Major element (wt%) composition of the bulk rock samples CB and AR, respectively, from the CBF and MAF

	Cabitza Fm.						Monte Argentu Fm.				
	CB1	CB3	CB4	CB15	CB28	CB29	AR2	AR5	AR11	AR14	AR15
SiO_2	60.31	55.12	59.70	59.54	62.50	59.88	58.81	57.57	57.43	62.07	62.77
TiO_2	0.87	1.05	1.03	0.74	0.92	0.96	0.87	0.91	0.96	1.07	1.05
Al_2O_3	19.92	23.57	21.45	20.41	20.20	21.67	20.23	20.64	20.91	21.04	20.62
Fe_2O_3tot	7.26	7.20	6.43	7.00	7.51	7.67	8.84	9.69	8.34	6.59	6.97
FeO	–	3.57	–	–	–	0.73	–	–	–	0.57	1.14
MnO	0.05	0.07	0.10	0.01	0.09	0.07	0.06	0.05	0.06	0.02	0.01
MgO	2.40	2.05	2.38	1.93	0.41	1.00	2.41	1.92	2.37	0.98	0.72
CaO	0.17	0.19	0.22	0.26	0.09	0.07	0.16	0.12	1.17	0.25	0.26
Na_2O	0.67	0.93	0.89	0.66	0.28	0.28	0.80	0.81	0.51	0.37	0.36
K_2O	3.76	4.04	3.79	5.06	4.40	4.66	3.42	3.73	3.94	3.81	3.68
P_2O_5	0.08	0.09	0.12	0.26	0.07	0.06	0.09	0.07	0.80	0.15	0.18
LOI	4.50	5.70	3.90	4.11	3.54	3.67	4.30	4.50	4.25	3.63	3.39

Where shown, the FeO was determined by colorimetric titration

of these minerals is comparable to that of the electron beam, and many of the analyses were consequently of a poor quality. On the basis of the structural formulas, we have considered and reported a selection of the best of these analyses in Tables 3 and 4. Potassic white mica has been analysed in three types of occurrences (1) detrital small crystals, (2) interleaving crystals with pyrophyllite and chlorite and (3) fine-grained (illite) crystals in the matrix which are mainly oriented as the pre-Variscan S_{1P} in the CBF samples and as the S_{1V} Variscan schistosity in the MAF samples. Two samples, one from the CBF (CB29) and one from the MAF (AR14), were analysed for their mica composition in great detail (Fig. 4). In CB29 (Fig. 4a), the Si content of the potassic white mica ranges between 6.01 and 6.57 a.p.f.u. The Fe and Mg increase from 0.18 to 0.49 a.p.f.u. and from 0.07 to 0.40 a.p.f.u., respectively, with increasing Si content. The Na content decreases from 0.20 to 0.01 a.p.f.u. In AR14 (Fig. 4b), a similar trend is observed, with the Fe and Mg content increasing from 0.15 to 0.33 and 0.10 to 0.40 a.p.f.u., respectively. The sodium content shows a negative trend, falling from 0.15 to 0.05 a.p.f.u., with a rising Si content (Si: 6.04–6.33 a.p.f.u.). The titanium levels vary from 0.02 to 0.14 a.p.f.u., but there is no correlation with the Si content. Some potassic white mica crystals are zoned, with an Fe–Mg-rich asymmetric core (FeO ~7, MgO ~2 wt%) surrounded by a discontinuous celadonite-poor rim (FeO ~1.5–2.5, MgO ~0.3–0.5 wt%). Although not systematic, the celadonite-poor mica with a low Mg and Fe content has commonly been observed in the fine-grained crystals in the matrix or in intergrowths with pyrophyllite, whereas the celadonite-rich mica has been observed in the detrital grains or single crystals in the matrix.

In the MAF samples, the chlorite is trioctahedral and di/trioctahedral (Fig. 5), with the former being the most abundant chlorite type. The trioctahedral chlorite in the samples from the CBF has an Al_{tot} content between 2.9 and 3.1 a.p.f.u. (based on 14 oxygen equivalents), Fe levels between 2.5 and 2.7 a.p.f.u., and X_{Mg} in the range 0.3–0.4. The trioctahedral chlorites have Al_{tot} in the 2.7–3.8 a.p.f.u. range, Fe from 1.9 to 2.3 a.p.f.u., and X_{Mg} mostly between 0.4 and 0.7. The di/trioctahedral chlorite always coexists with pyrophyllite. In the interleaving of the mineral aggregates from samples AR14 and AR15, a Zn-rich variety of di/trioctahedral chlorite (Zn sudoite, ZnO up to 3.1 wt%, Zn ~0.2 a.p.f.u., X_{Mg} ~0.70) was also found (Cruciani et al. 2015b), along with potassic white mica and pyrophyllite (Table 4).

In the very low-grade metaclastites of the Betic Cordillera (Spain), Ruiz Cruz and Sanz de Galdeano (2005) described a wide variety of sudoite mixed layered structures consisting of illite–sudoite, pyrophyllite–sudoite and dickite–sudoite, which were investigated by XRD and transmission/analytical electron microscopy. We investigated phyllosilicate intergrowths from two selected microdomains from sample AR14 and two from sample AR15 using TEM, EDS microanalyses, and selected area electron diffraction. In the selected microdomains, which were specifically chosen on the basis of the occurrence of the phyllosilicate intergrowths, phyllosilicates widely occur at the boundary of other matrix phases such as quartz and Fe oxides. The following phyllosilicate types have been identified in the interleavings, with an alternation of 10- to 20-nm-thick lamellae (Fig. 6a, b): (1) pyrophyllite-type lamellae with a ~9 Å periodicity along the c* axis; (2) muscovite-type lamellae with a ~10 Å periodicity along c*; and (3) sudoite-type lamellae with a ~14 Å periodicity along the same direction. EDS analyses of the 14 Å lamellae revealed the systematic occurrence of zinc in the crystal lattice of the sudoite. No mixed layered structure in the sudoite was found (Fig. 6c, d). The average composition of the 14 Å

Table 3 Selected microprobe analyses of potassic white mica from the CBF and MAF samples (CB and AR, respectively)

	Cabitza Fm.					Monte Argentu Fm.					
	CB3		CB29			AR14			AR11	AR4	
	D	M	M	I	D	M	I	D	M	D	M
SiO_2	46.56	45.38	45.44	46.74	48.38	45.94	46.86	46.72	45.96	45.61	45.90
TiO_2	0.56	0.15	0.25	0.06	0.30	0.28	0.38	0.49	1.28	0.93	1.16
Al_2O_3	28.70	34.77	36.80	35.89	29.03	36.75	35.04	28.60	30.98	29.85	34.81
FeO	2.32	1.14	1.60	1.69	3.79	1.69	1.45	2.67	2.55	2.74	1.51
Fe_2O_3	3.45	1.30	–	–	–	–	–	4.34	2.24	2.99	–
MnO	–	–	–	–	0.03	–	–	0.01	0.00	–	–
MgO	2.25	1.37	0.75	0.34	2.01	0.72	1.07	2.00	1.92	1.61	1.03
CaO	–	0.05	–	–	–	0.02	0.01	0.02	0.05	0.04	0.04
Na_2O	0.16	0.47	0.23	0.44	0.03	0.23	0.65	0.15	0.24	0.13	0.32
K_2O	10.68	10.21	10.49	9.42	11.00	10.79	9.79	10.99	10.33	10.61	10.38
BaO	0.23	0.15	0.25	0.40	0.02	0.35	0.22	0.43	1.18	–	–
F	0.17	–	0.10	–	–	0.19	0.08	0.17	–	–	–
H_2O	4.31	4.48	4.49	4.54	4.42	4.47	4.50	4.34	4.47	4.38	4.51
Total	99.39	99.47	100.40	99.52	99.01	101.43	100.05	100.93	101.20	98.89	99.66
Si	6.35	6.07	6.01	6.18	6.57	6.04	6.19	6.33	6.17	6.24	6.11
Al	4.62	5.47	5.74	5.58	4.64	5.69	5.45	4.57	4.90	4.81	5.45
Ti	0.06	0.02	0.02	0.01	0.03	0.03	0.04	0.05	0.13	0.10	0.11
Fe^{2+}	0.26	0.12	0.18	0.19	0.43	0.19	0.16	0.30	0.29	0.31	0.17
Fe^{3+}	0.35	0.13	–	–	–	–	–	0.44	0.23	0.31	–
Mn	–	–	–	–	0.00	–	–	0.00	–	–	–
Mg	0.46	0.27	0.15	0.07	0.41	0.14	0.21	0.40	0.38	0.33	0.20
Ca	–	0.01	–	–	–	0.00	0.00	0.00	0.01	0.01	0.01
Na	0.04	0.12	0.06	0.11	0.01	0.06	0.17	0.04	0.06	0.03	0.08
K	1.86	1.74	1.77	1.59	1.90	1.81	1.65	1.90	1.77	1.85	1.76
Ba	0.01	0.01	0.01	0.02	0.00	0.02	0.01	0.02	0.06	–	–
F	0.07	–	0.04	–	–	0.08	0.03	0.07	–	–	–
H	3.93	4.00	3.96	4.00	4.00	3.92	3.97	3.93	–	4.00	4.00
X_{Mg}	0.63	0.69	0.45	0.26	0.49	0.43	0.57	0.57	0.57	0.52	0.54
Na/Na + K	0.02	0.06	0.03	0.07	0.01	0.03	0.09	0.02	0.03	0.03	0.03

D detrital white mica, *I* white mica in interleaving and *M* white mica from the matrix

phyllosilicate lamellae is $SiO_2 = 38.39$ (wt%), $TiO_2 = 0.09$, $Al_2O_3 = 39.47$, FeO = 8.30, MgO = 9.88, ZnO = 3.82 and $K_2O = 0.05$, which is very similar to that obtained by the electron microprobe (EMP) analyses shown in Table 4.

The paragonite of the CBF shows a Si content of ~6.2 a.p.f.u., X_{Mg} ~0.4 and Na/(Na + K) ~0.7. In the MAF, the paragonite has Si level of 6.2 a.p.f.u., slightly higher X_{Mg} (0.5) and slightly higher Na/(Na + K) ~0.84. Crystals with variable Na/K ratios, which are probably referable to Na–K mica, have also been found in the CBF and MAF rocks. In sample AR11 from the MAF, we also found in the rock matrix very fine-grained crystals with a semi-quantitative composition that is very similar to that of biotite (K_2O 9.98, MgO 19.37, FeO 10.75, Al_2O_3 15.15, and SiO_2 38.94). However, the very small size of these crystals did not allow us to conduct quantitative analyses.

Pyrophyllite and kaolinite were identified by XRD as well as by wavelength-dispersive spectroscopy analyses. The latter reveals that pyrophyllite and kaolinite are almost pure mineral phases. Small amounts of FeO (0.66 wt%) and trace amounts of Mn and Mg were sometimes detected in the pyrophyllite.

Geothermobarometry

Illite crystallinity and chlorite crystallinity indexes

The IC was determined in the mica fraction <2 μm. The results obtained refer to the S_{1P} pre-Variscan schistosity in the CBF and to the S_{1V} Variscan schistosity in the MAF.

Table 4 Selected microprobe analyses of chlorite and sudoite from the CBF and MAF samples (CB and AR, respectively)

	Cabitza Fm.				Monte Argentu Fm.						
	CB1	CB3	CB7	CB27	AR4	AR11	AR12	AR16	AR14		AR15
	Chl	Chl	Chl	Chl	Chl	Chl	Chl	Chl	Sud	Zn-Sud	Zn-Sud
SiO_2	25.06	25.11	24.68	25.86	25.90	25.93	25.13	24.30	36.03	35.96	33.27
TiO_2	0.03	0.06	–	0.06	0.06	0.10	0.04	0.01	0.08	–	–
Al_2O_3	23.56	23.90	24.69	23.57	23.99	22.23	24.20	23.60	35.13	34.68	35.53
FeO_{tot}	29.75	30.69	30.36	27.96	26.66	22.39	25.94	29.40	6.24	6.40	6.72
MnO	0.13	0.32		0.03	0.03	0.09	0.70	0.20	0.01	–	–
MgO	9.86	9.79	9.27	10.93	12.09	17.44	12.75	10.03	7.88	8.10	9.39
CaO		–	–	–	–	–	–	–	–	–	–
Na_2O		–	–	–	–	–	–	–	–	–	–
K_2O		–	–	–	–	–	–	–	–	0.22	0.20
ZnO		–	–	–	–	–	0.05	–	–	3.07	2.96
Total	88.39	89.87	89.00	88.41	88.73	88.19	88.81	87.54	85.36	88.43	88.07
Si	2.67	2.64	2.61	2.72	2.69	2.67	2.62	2.62	3.33	3.29	3.08
Al	2.96	2.96	3.08	2.92	2.94	2.69	2.97	2.99	3.83	3.74	3.88
Ti	0.00	0.00	–	0.00	0.01	0.01	0.00	0.00	0.01	–	–
$Fe^{2+}tot$	2.65	2.70	2.69	2.46	2.32	1.93	2.26	2.65	0.48	0.49	0.52
Mn	0.01	0.03	–	0.00	0.00	0.01	0.06	0.02	0.00	–	–
Mg	1.57	1.54	1.46	1.71	1.87	2.67	1.98	1.61	1.09	1.10	1.30
Ca	–	–	–	–	–	–	–	–	–	–	–
Na	–	–	–	–	–	–	–	–	–	–	–
K	–	–	–	–	–	–	–	–	–	0.02	0.02
Zn	–	–	–	–	–	–	0.00	–	–	0.21	0.20
X_{Mg}	0.37	0.36	0.35	0.41	0.45	0.58	0.47	0.38	0.69	0.69	0.71

The CBF samples yielded IC values in the range 0.24–0.36 Δ°2θ, with 18 of 24 samples falling in the range 0.26–0.32 Δ°2θ. The average IC value was 0.29 Δ°2θ (Fig. 7a). The MAF samples are characterized by IC values in the range 0.26–0.42 Δ°2θ, with 10 of 22 samples plotting in the range 0.32–0.38 Δ°2θ. The average value of the IC was 0.35 Δ°2θ (Fig. 7b). Both sets of values indicate anchizone metamorphism.

The same difference in behaviour between the two sample groups was also observed for the chlorite crystallinity. The chlorite crystallinity values yielded by the CBF samples are in a range from 0.18 to 0.30 Δ°2θ, with a cluster of values between 0.18 and 0.24 Δ°2θ (Fig. 7c). Samples from the MAF show a cluster of values between 0.18 and 0.22 Δ°2θ (Fig. 7d). The difference between the values observed in the two groups could be explained by the variable content of the detrital chlorite.

The b_0 value of potassic white mica

The CBF samples (Fig. 7e) have b_0 values between 8.976 and 9.042 Å (average 9.009 Å), with 17 of 23 samples clustering between 8.994 and 9.030 Å. The MAF samples (Fig. 7f) are characterized by b_0 values between 8.988 and 9.036 Å (average 9.008 Å), with a cluster of values (18 samples out of 20) in the 8.994–9.018 Å range. The large spread of values yielded by the two groups must be ascribed to the variable contribution of both the authigenic and inherited detrital potassic white mica.

P–T pseudosections

In order to show the relationships between the bulk chemistry of the rock and mineral assemblages, we calculated P–T pseudosections with the software package Perple_X 6.6.9, following the approach of Connolly (1990), with the internally consistent thermodynamic dataset and equation for H_2O of Holland and Powell (1998, revised 2004). The P–T pseudosections were calculated for AR14 sample from the MAF and the CB29 sample from the CBF using the bulk rock compositions determined by XRF (Table 2). The compositions were normalized to 100 % after disregarding P (mostly contained in apatite) Ca, Mn and LOI. The samples are characterized by a low FeO content and, consequently, a high XFe_2O_3 (i.e. Fe_2O_3/Fe_2O_3tot) ratio (Table 2). The phases considered in the calculation were white mica, chlorite, sudoite (Sud), kaolinite, pyrophyllite,

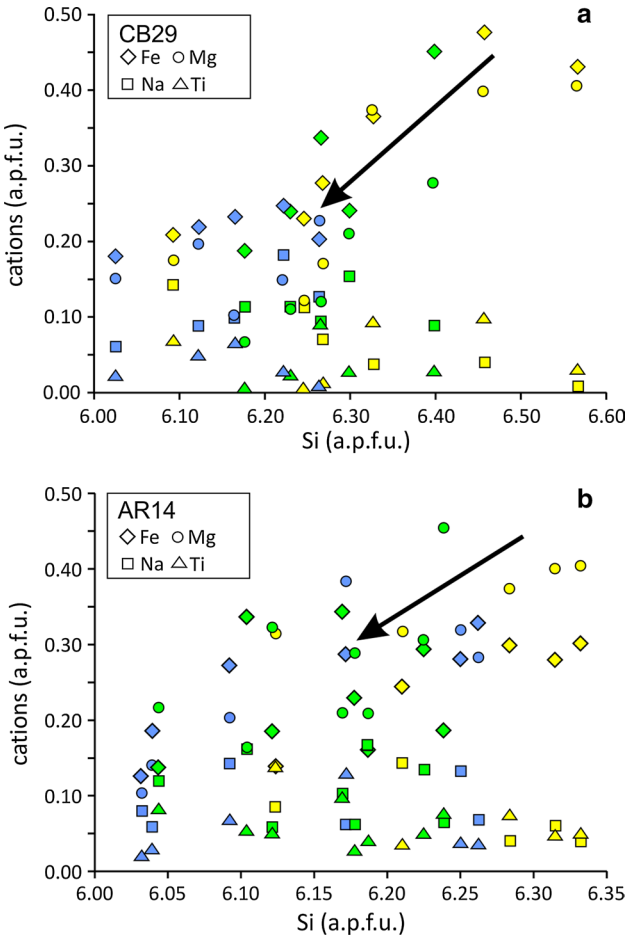

Fig. 4 Compositional variations of potassic white mica of (**a**) the CBF sample CB29 and (**b**) the MAF sample AR14 in terms of Fe, Mg, Na and Ti vs. the Si content (a.p.f.u.). Symbols: *yellow*, detrital K-white mica; *green*, K-white mica in interleaving; *blue*, K-white mica in the matrix mainly oriented as pre-Variscan S_{1P} in the CBF and S_{1V} Variscan in the MAF. Additional analyses not reported in Table 3 are also shown

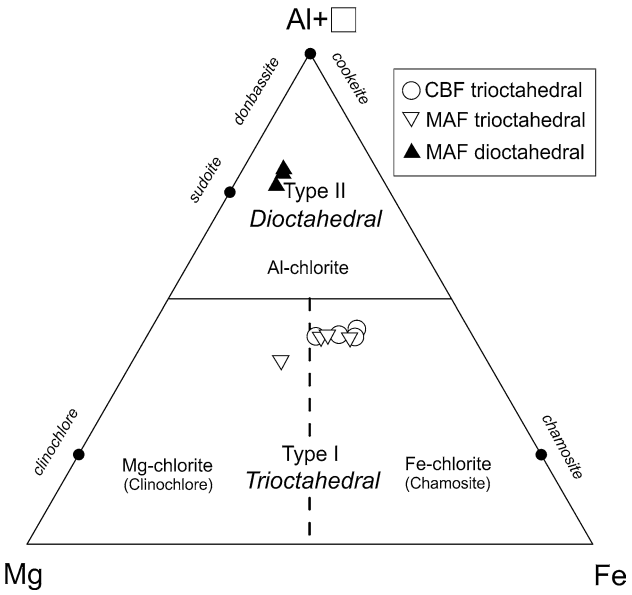

Fig. 5 Ternary Al + vacancy–Fe–Mg classificative *diagram* for chlorites following Zane and Weiss (1998)

chloritoid, carpholite, Al–silicate, cordierite, haematite, magnetite, rutile and quartz. The solid solution models are those of Holland and Powell (1998) for muscovite and epidote, Holland et al. (1998) for chlorite and Massonne and Willner (2008) for carpholite, while an ideal model was used for Mg–Fe sudoite. An ideal ilmenite–geikielite–pyrophanite solid solution model was also used. The pseudosection calculated with a $H_2O = 1$ and all iron as FeO (not shown) predicts the occurrence of chloritoid (not observed in our samples) in most of the multivariant P–T fields, but does not envisage the coexistence of potassic white mica and pyrophyllite. This result disagrees with the observed paragenesis (i.e. the absence of chloritoid and the coexistence of potassic white mica and pyrophyllite in the studied sample) and confirms the observation that neglecting ferric iron in greenschist facies assemblages may led to thermodynamic modelling that reproduces neither the observed mineral assemblage nor the measured mineral compositions (Lo Pò and Braga 2014). The pseudosections calculated with the actual XFe_2O_3 ratios for samples AR14 and CB29 (Figs. 8a, 9a) with $aH_2O = 1$ indicate that the observed mineral assemblage is stable below 0.6 GPa at ~300–400 °C. These values refer to S_{1P} pre-Variscan minerals in the CBF and S_{1V} Variscan schistosity in the MAF. Using the ideal solution model for sudoite, this mineral was found to not be stable in the P–T range of interest. Sudoite is predicted to be stable at high temperatures in the P–T range of interest when the sudoite solution model by Massonne and Willner (2008) is used. However, in this latter case, the temperatures for the appearance of Fe sudoite appear to be quite high. In order to ascertain the influence of XFe_2O_3 on the stability of the mineral assemblages, we calculated a T–XFe_2O_3 pseudosection for each sample (Figs. 8b, 9b) at 0.3 GPa within the temperature range 200–500 °C. Potassic white mica + chlorite coexist from the lowest values of the XFe_2O_3 ratios, whereas the pyrophyllite is stable for $XFe_2O_3 > 0.2$. In the $0.2 \leq XFe_2O_3 \leq 0.8$ range, chlorite, pyrophyllite and white mica also coexist with chloritoid, which in turn disappears at $XFe_2O_3 \geq 0.8$. Carpholite is stable in the 270–320 °C range at high oxidizing conditions ($XFe_2O_3 > 0.85$). At a lower pressure (0.2 GPa), the P–T pseudosection topology does not change greatly, but the carpholite stability field is greatly reduced, while that of andalusite becomes wider. Calculations with a higher pressure (0.5 GPa) do not significantly change the topology and mineralogical assemblages of the multivariant P–T fields of the P–T pseudosection. The T–XFe_2O_3

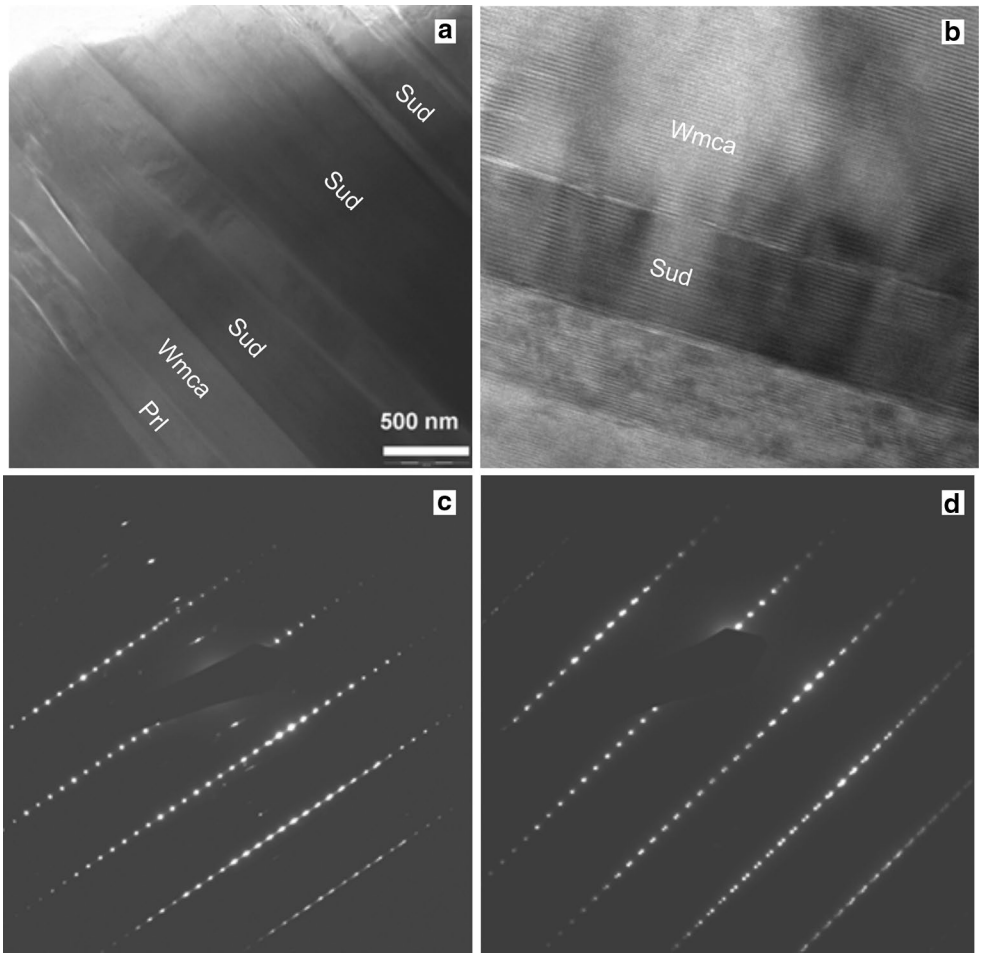

Fig. 6 **a**, **b** TEM medium magnification image from sample AR14, showing an alternation of pyrophyllite-type, muscovite-type and sudoite-type lamellae; **c**, **d** the lattice fringe images of sudoite show a regular 14 Å periodicity

pseudosections (Figs. 8b, 9b) reveal that the potassic white mica + pyrophyllite + chlorite + paragonite assemblage only occurs in oxidized conditions (XFe_2O_3 > 0.8–0.9). It is worthy of note that the XFe_2O_3 ratio of the samples is quite similar to that predicted by the T–XFe_2O_3 pseudosections for the first appearance of pyrophyllite in the mineral assemblage. This could mean that the XFe_2O_3 ratio of the samples probably approximates that of the rock at the time of the metamorphism.

P–T conditions

Low-temperature P–T conditions in the MAF and CBF are constrained by the occurrence of pyrophyllite. Pyrophyllite replaces kaolinite at about 300 °C according to the reaction Kln + 2 Qtz = Prl + H_2O (Bucher and Grapes 2011, 263). At about 400 °C, pyrophyllite decomposes to Al–silicate + Qtz in the presence of pure H_2O fluid according to the reaction Prl = Als + 3Qtz + H_2O. Pyrophyllite is often present in the MAF samples but was restricted to those from the SE of the Monte Anna locality in the CBF samples (Fig. 1). The kaolinite occurrence requires further explanation. In the studied samples, kaolinite was usually observed in the pyrophyllite-free samples. It only coexists with pyrophyllite in samples CB28–29. Kaolinite in coexistence with pyrophyllite can be tentatively regarded as prograde, whereas that detected in the pyrophyllite-free samples is likely to be retrograde. The empirical chlorite solid solution geothermometer as a function of the Al^{IV} (a.p.f.u.) content (calibration I by Cathelineau and Nieva 1985) and octahedral vacancy (calibration II) yielded temperatures from 285–308 and 238–251 °C for the matrix blastic trioctahedral chlorites from the CBF. The same calibrations yielded values in the 291–307 and 206–276 °C ranges for the matrix blastic chlorites of the MAF rocks. The Lanari et al. (2014) calibration of the chlorite geothermometer yielded values of 220–281 °C in the rocks from the CBF and 230–302 °C in the MAF samples. The exception was sample AR11 with 502 °C. Higher temperatures were obtained by

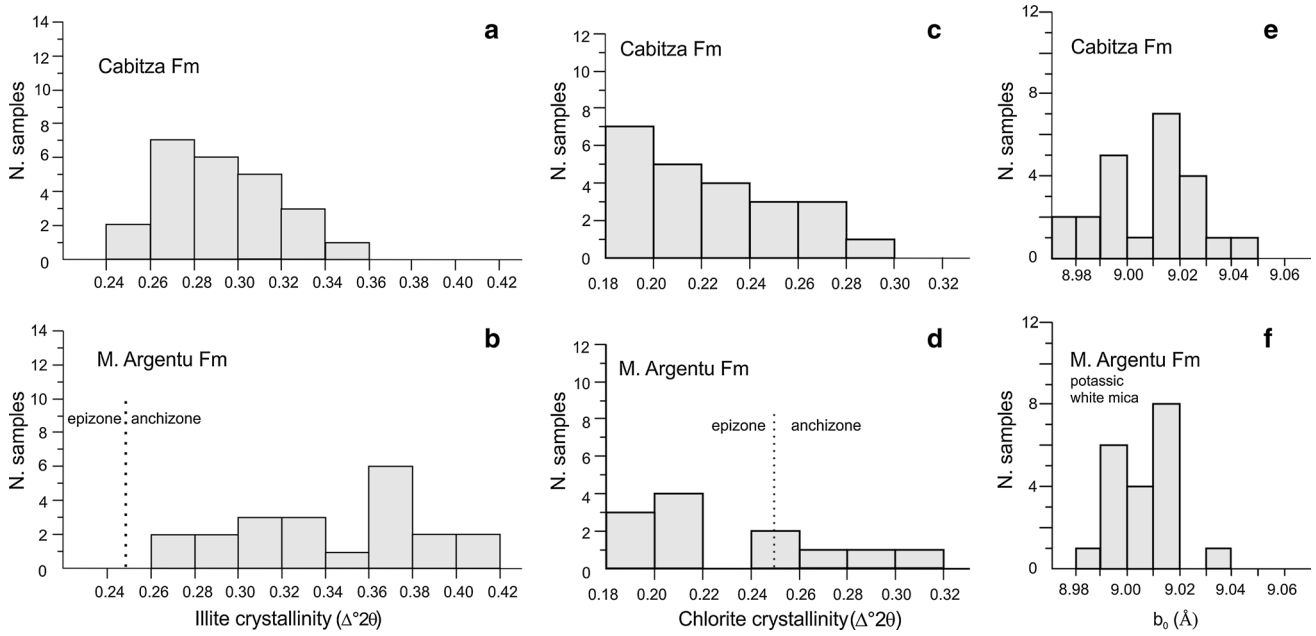

Fig. 7 **a**, **b** Distribution of the illite crystallinity index (Kubler index, Δ°2θ) for the CBF and MAF samples. The boundary between the epizone and anchizone is also shown; **c**, **d** distribution of the chlorite crystallinity index (7 Å peak, 002, Δ°2θ) for the CBF and MAF samples. The boundary between the epizone and anchizone is also shown; **e**, **f** distribution of the b_0 spacing (Å) of potassic white mica for the CBF and MAF samples

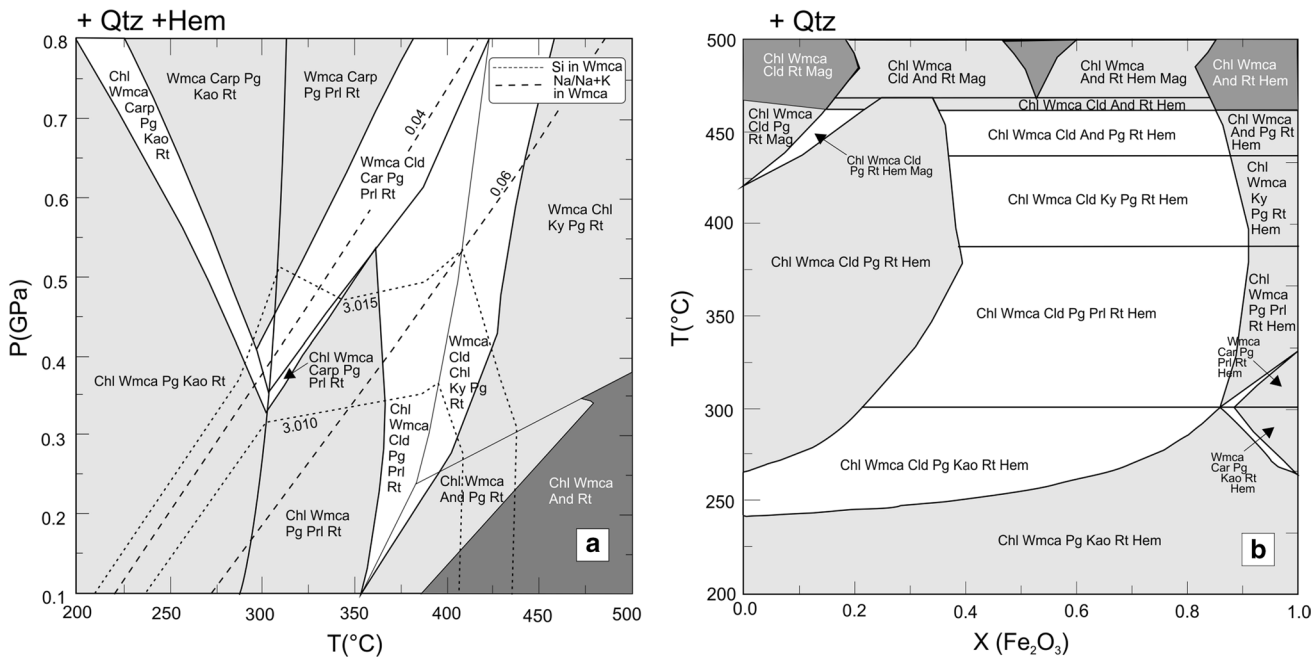

Fig. 8 P–T pseudosection modelling for sample AR14 of the MAF: **a** P–T pseudosection in the 200–500 °C, 0.1–0.8 GPa range calculated for the bulk composition determined by XRF and for XFe_2O_3 (0.89) determined by titration. Some selected isopleths showing the Si content (atoms per half formula unit, a.p.h.f.u.) and the Na/Na + K ratio for potassic white mica (Wmca) are also shown; and **b** T–XFe_2O_3 pseudosection calculated at $P = 0.3$ GPa between 200 and 500 °C

the application of the Cathelineau (1988) calibration of the chlorite geothermometer, which has a general applicability in diagenetic, hydrothermal and metamorphic settings. With this calibration, we obtained temperatures in the 351–385 °C range for the CBF chlorites and 359–384 °C for those from the MAF. Comparable temperature values,

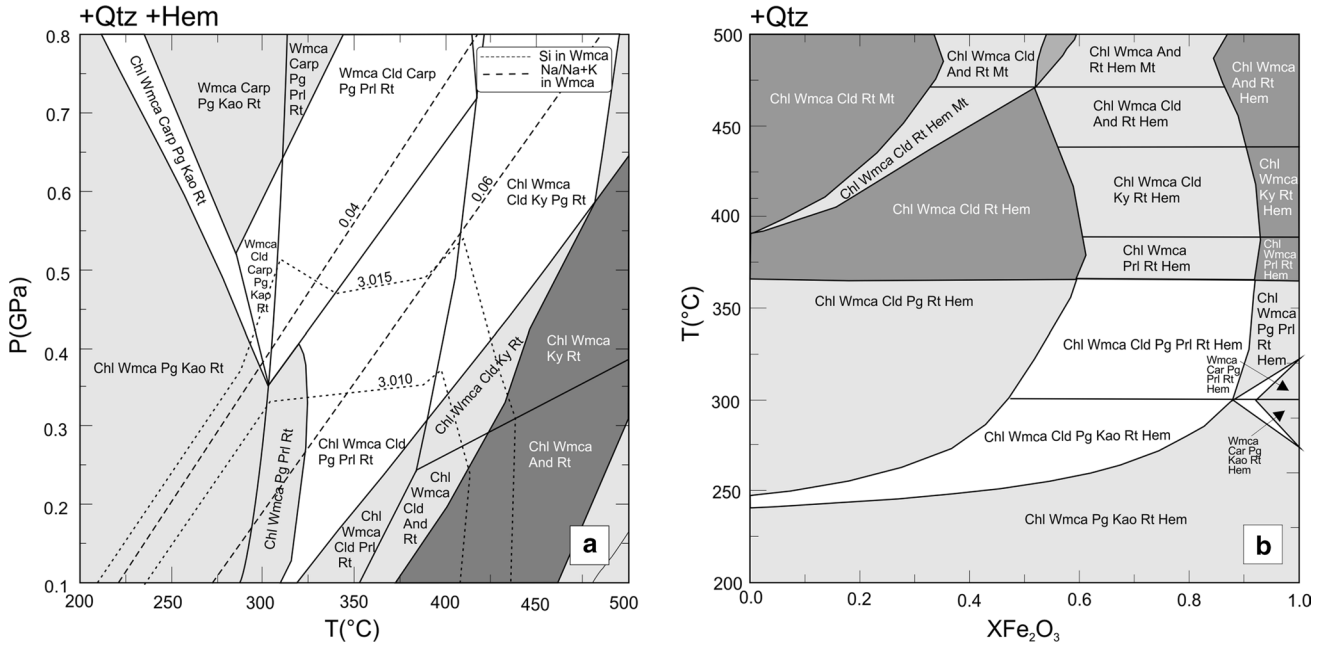

Fig. 9 P–T pseudosection modelling for sample CB29 of the CBF: **a** P–T pseudosection in the 200–500 °C, 0.1–0.8 GPa range calculated for the bulk composition determined by XRF and for XFe_2O_3 (0.89) determined by titration. Selected isopleths showing the Si content (a.p.h.f.u.) and the Na/Na + K ratio for potassic white mica (Wmca) are also shown; and **b** T–XFe_2O_3 pseudosection calculated at $P = 0.3$ GPa and 200–500 °C

in the range 314–367 °C for the CBF and 327–365 °C for the MAF, were given by the Hillier and Velde (1991) chlorite geothermometer, which is a formulation that is suitable for low-temperature chlorites. The P–T conditions of the pyrophyllite-bearing samples from the MAF can be further constrained by the P–T pseudosection approach. The pseudosections calculated with the actual XFe_2O_3 ratio for sample AR14 (Fig. 8a), with a $H_2O = 1$, indicate that the observed mineral assemblage is stable below 0.6 GPa, at 300–400 °C. In order to place some constraints on the metamorphic pressure, we calculated compositional isopleths for the Si content (a.p.f.u.) and the Na/(Na + K) ratio in potassic white mica (Fig. 8a). These isopleths cross the stability field of pyrophyllite, with Si values from 3.01 to 3.02 a.p.f.u. In the studied sample, the Si content of the potassic white mica ranges from 6.04 to 6.33 a.p.f.u. (22 oxygens). The modelled isopleths also suggest that potassic white mica in equilibrium with pyrophyllite should have a Na/(Na + K) ratio between 0.04 and 0.07, in very good agreement with the determined values. Very similar results were obtained from a P–T pseudosection calculation in sample CB29 from the CBF (Fig. 9). The arrows in Fig. 4 join the detrital potassic white mica with the potassic white mica from interleaving, representing the change in chemical composition during the rock metamorphic re-equilibration. The observation that potassic white mica in the pyrophyllite interleaving is celadonite-poor means that newly formed (or re-equilibrated) potassic white mica is mainly controlled by the bulk chemistry of the rock and that it is independent of the detrital potassic white mica composition. Furthermore, the fact that we find potassic white mica with a chemical composition that contrast with the observed paragenesis (celadonite-rich potassic white mica in Al-rich system) suggests that the detrital potassic white mica is not equilibrated and retains the original pre-metamorphic composition. In other words, we interpret the celadonite-poor potassic white mica as being in equilibrium with the metamorphic assemblage, whereas the celadonite-rich mica is not. Franceschelli et al. (1991) described interleavings made up of phyllosilicate growing on detrital potassic white mica in the Verrucano rocks from the Northern Apennines. According to these authors, the detrital potassic white mica grains provided sites for the formation of metamorphic minerals, meaning that there is a relationship between the process of mica re-equilibration and the local composition of interleaving phyllosilicate grains. A similar process can be proposed for the formation of the phyllosilicate interleavings in the Iglesiente rocks (Cruciani et al. 2015b). Potassic white mica re-equilibration occurred through mass transfer and a chemical exchange with a fluid phase in equilibrium with the mineral association of the rock matrix. The model of the intergrowth formation from the detrital potassic white mica grains can possibly also be extended to chlorite in the studied rocks. The occurrence

of zinc in the interleavings of our samples probably derives from the presence of other zinc-rich phases (i.e. gahnite) in the rocks. In conclusion, for the potassic white mica + pyrophyllite + chlorite assemblage of the MAF, the Si content of potassic white mica in the intergrowth with the pyrophyllite (3.01–3.02 a.p.f.u.) allows us to estimate the P–T conditions of 0.3–0.5 GPa, 300–350 °C. However, the sporadic occurrence of kaolinite seems to suggest that the metamorphic temperatures are closer to 300 °C than 350 °C and considering the lowest Si content of K-white mica near to 0.3 GPa.

Discussion

Comparison of the metamorphic grade attained by the CBF and MAF

The two groups of samples from the CBF and MAF contain phyllosilicates from kaolinite to pyrophyllite and potassic white mica that correspond to different temperature ranges. The only difference between the two groups is provided by the ranges of the IC values for illite: from 0.24 to 0.36 in the CBF and from 0.26 to 0.42 in the MAF.

The CBF is homogeneous, with a maximum frequency at 0.26–0.28 downgrading towards 0.24 and 0.36. The MAF is heterogeneous and divided into two subgroups of values: 0.26–0.34 and 0.34–0.42, with a significant peak at 0.36–0.38. The highest frequency of low IC values in the CBF and, in particular, the remarkable difference in the range of peak values could be roughly interpreted as an indication of a slightly higher metamorphic grade in the CBF than the MAF.

However, the slight difference in IC values between the underlying CBF and the overlying MAF can more probably be ascribed to different factors such as lithology, bulk chemistry and the degree of chemical re-equilibration.

The IC values for chlorite show similar, but less accentuated, behaviour: higher percentages of low values in the entire set of data for the CBF and two distinct populations of data for the MAF. As regards the b_0 values, the discrepancies between the two groups could only be due to a different abundance of detrital potassic white mica, particularly in the CBF, which shows a wider range of values (8.976–9.042 Å), i.e. greater heterogeneity if compared to the AR values (8.988–9.036 Å). Finally, the P–T conditions of metamorphism estimated by the P–T pseudosection approach are almost identical for both groups. The b_0 values and geothermobarometric results do not reveal a significant difference in the P–T conditions between the formations below and above the Sardic unconformity.

We suggest that the Sardic phase in the CBF is probably associated with an Ordovician low- to very low-grade metamorphism related to the older pre-Variscan S_{1P} schistosity and comparable to the Variscan metamorphism in the MAF.

The age of the Variscan deformation and metamorphism in the Sulcis–Iglesiente is not well constrained. The only available data are stratigraphic. In the External and External Nappe zones, the younger formations, which underwent thrusting, folding and Variscan metamorphism, are Early Carboniferous in age (Corradini et al. 2003), whereas the oldest formations not involved in deformation and metamorphism are those of the Late Carboniferous–Early Permian basins (Barca et al. 1995; Pittau et al. 2008).

Sardic unconformity in the geodynamic frame of the pre-Variscan North Gondwana margin

The first comprehensive geodynamic model of the evolution of Variscan Sardinia within the frame of the pre-Variscan North Gondwana margin from the Cambrian to the Carboniferous was provided by Carmignani et al. (1994, 2001). According to these authors, the Sardic Phase may be interpreted as being associated with a back-arc compression that is related to the development and progressive migration of the magmatic arc towards the SW in the Middle Ordovician.

New geodynamic models enriching the one conceived by Carmignani et al. (1994, 2001) have recently been put forward by Rossi et al. (2009, Fig. 5), Oggiano et al. (2010, Fig. 8) and Gaggero et al. (2012). Taking into account the quite similar steps identified in these three models, a synthesis of the geodynamic evolution of the North Gondwana margin between the Upper Cambrian and the Ordovician–Silurian boundary can be proposed as follows: (1) a pre-Sardic volcanic cycle with the emplacement of felsic transitional volcanites in the Upper Cambrian–Early Ordovician time span; (2) a Lower Ordovician opening of the Rheic Ocean between Gondwana and Laurussia or between Hun Superterrane and Gondwana; (3) a subduction of the Rheic Ocean beneath the northern continental margin of Gondwana with the consequent generation of a calc-alkaline magmatism in Sardinia during the Middle Ordovician; (4) thereafter, a rifting stage that affected the volcanic arc since the Middle Ordovician and gave rise to an alkaline magmatism and the opening of the Palaeo-Tethys Ocean at the Late Ordovician–Early Silurian boundary; and (5) back-arc spreading and progressive oceanization from the Early Silurian up to the Late Silurian and Devonian.

A more complex framework is depicted by von Raumer et al. (2013, Fig. 4, Table 1 and references therein). In their reconstruction, the part of Sardinia with more widespread Lower to Middle Ordovician acidic calc-alkaline volcanic rocks is placed near Sicily, while the Lower Ordovician acidic gneisses of Northern Sardinia, together with the

Middle–Upper Ordovician calc-alkaline gabbros of Eastern Maures, the Middle Ordovician orthogneisses of the Montagne Noire, and the Lower to Middle Ordovician granitoids and gabbros of the Pyrenean Belt, are located in a more southern position (see Fig. 4 and ages in Table 1 of von Raumer et al. 2013). In any case, Maures, Montagne Noire and the Pyrenean Belt are strictly correlated to Sardinia.

Comparison with other Palaeozoic unconformities in the European Variscides

Comparing the Sardic Unconformity with similar unconformities within the South Variscan Realm can contribute to the reconstruction of the Ordovician palaeogeography of Sardinia. Save for the article by Linnemann and Romer (2002), which used chemical and isotopic analyses to differentiate between the rocks below and above an unconformity embracing the Lower Ordovician, our paper is the only one to use bulk rock chemistry and metamorphic parameters such as b_0, IC and CI to ascertain the possible significant differences between the two formations below and above the Sardic unconformity. All the other papers dealing with the Sardic unconformity are based on tectonics, structural geology, lithostratigraphy, and palaeogeographic and geodynamic reconstructions. These differences in approach preclude any possibility of comparing our metamorphic data with non-existent similar data from other papers. Only Casas (2010) provides some hint at metamorphism. In the case of the Canigó Massif (easternmost Pyrenean Belt), this author recognized that "Upper Ordovician and Cambro-Ordovician metasediments are affected only by weak metamorphism" and that "the Ordovician deformation is moderate without cleavage formation", which are features also characterizing the CBF and MAF.

The other places in which the Sardic unconformity has been observed are Iberia, Armorica, the Pyrenean Belt and Montagne Noire (Álvaro et al. 2016) on the southern side of the French Massif Central, and Saxo-Thuringia. A thorough discussion of the Sardic phase in Iberia was provided by Lefort (1989), who observed a gradual increase in the angle of the Sardic unconformity from the Central Iberian Zone (CIZ) towards the Ossa Morena Zone (OMZ) and, more recently, by Correia Romão et al. (2005). According to the latter authors, the Sardic deformation was produced by an early drifting of Armorica/Hun terranes from Gondwana. Owing to the complexity of an intracratonic rifting event, the related deformation should be diachronic on the plate tectonic scale. In the CIZ, the rift and related deformation started between the Upper Cambrian and Arenig and then, during the Ordovician, migrated to the SW in the OMZ. The analogies between the Sardic phase in Iberia and Sardinia are: (1) the presence of the same strong angular unconformity prior to the Variscan deformation; (2) the occurrence of coarse conglomerates with a red silt-pelitic matrix above the unconformity; and (3) the interference between orthogonal Sardic and Variscan folds (D_2 phase), generating a basin and dome pattern. However, Iberia and SW Sardinia have some different elements when it comes to the Sardic deformation and the entire sequence above and below the Sardic unconformity. In Iberia, the Sardic phase is older and took place between the Cambrian and the Tremadoc. In SW Sardinia, the Sardic deformation is younger and attributed to the Middle Arenig–Caradoc interval. In Iberia, two pre-Variscan unconformities are distinguished: a first, high angle, unconformity between the Proterozoic–Cambrian sequence and a volcano-sedimentary sequence that is Tremadoc–Lower Arenig in age. A second, weaker, low-angle unconformity between this sequence and the overlying Armorican Quartzite Formation is Upper Arenig in age. In SW Sardinia, only one unconformity was found between the Middle Arenig and Caradoc sequences.

Concluding remarks

Field survey and new data from mineralogy, petrography and mineral chemistry on rock samples from the CBF and MAF cast new light on the geology and metamorphism of rocks above and below the Sardic unconformity. The following findings were obtained:

1. The new tectonic evidence on Ordovician tectonics for the key locality of SW Sardinia reveals that the Sardic unconformity covers older pre-Variscan structures such as overthrust, km-sized folds and reverse faults.
2. The IC data clustering to lower values in the CBF and higher values in the MAF may suggest a slightly higher metamorphic grade of the former. However, the local occurrence of detrital white mica and the wide overlapping of the IC values between the two groups of samples, both of which plot in the anchimetamorphic field, render this conclusion doubtful.
3. Very similar ranges of the b_0 values suggest that both formations underwent a comparable metamorphic pressure, while the slightly greater heterogeneity of the CBF b_0 values could indicate a higher content of detrital potassic white mica in the CBF samples.
4. No significant differences in the metamorphic grade between the two groups of samples were revealed by the P–T pseudosections.

Acknowledgments The authors wish to thank Dr. E. Sarria (ARPAS, Sardegna) for the assistance provided during the development of this research. The reviews of R. Braga (University of Bologna) and G. Oggiano (University of Sassari) and of the guest editor P. Pitra (University of Rennes) were constructive and helped to improve the paper. This work has been carried out within the framework of the CARG mapping project L. 226/99 (funds to M. Franceschelli). Contributo di

Ateneo alla Ricerca (CAR, PRID 2015) funds (Università di Cagliari) are also acknowledged. We also wish to thank Cecilia Viti (University of Siena) for the TEM analyses.

References

Álvaro JJ, Colmenar J, Monceret E, Pouclet A, Vizcaïno D (2016) Late Ordovician (post-Sardic) rifting branches in the North Gondwanan Montagne Noire and Mouthoumet massifs of southern France. Tectonophysics 681:111–123

Arthaud F (1963) Un exemple de tectoniques superposées dans le Paléozoique de l'Iglesiente (Sardaigne). CR Soc Géol France 9:303–304

Arthaud F (1970) Étude tectonique et microtectonique comparée de deux domaines Hercyniens: Les nappes de la Montagne Noire (France) et l'anticlinorium de l'Iglesiente (Sardaigne). Publications de l'Université des Sciences et Techniques du Languedoc-Série Géologie Structurale 1, Montpellier, p 175

Barca S, Carmignani L, Eltrudis A, Franceschelli M (1995) Origin and evolution of the Permian-Carboniferous basin of Mulargia Lake (South-Central Sardinia, Italy) related to the Late-Hercynian extensional tectonic. CR Acad Sci Paris 321(IIa):171–178

Brandelik A (2009) CALCMIN–an EXCEL™ Visual Basic application for calculating mineral structural formulae from electron microprobe analyses. Comput Geosci 35:1540–1551

Brower H (1987) The Sardic tectonic phase in SW Sardinia: a concept rejected. IGCP n.5 Newsletter 7:134–138

Bucher K, Grapes R (2011) Petrogenesis of Metamorphic Rocks, 8th edn. Springer-Verlag, Berlin Heidelberg, p 428

Carmignani L, Cocozza T, Gandin A, Pertusati PC (1982) Lineamenti della geologia dell'Iglesiente-Sulcis. In: Carmignani L, Cocozza T, Ghezzo C, Pertusati PC, Ricci CA (eds), Guida alla Geologia del Paleozoico Sardo. Guide Geologiche Regionali: Roma, Soc Geol It, pp 65–77

Carmignani L, Cocozza T, Gandin A, Pertusati PC (1986) The Geology of Iglesiente. In: Carmignani L, Cocozza T, Ghezzo C, Pertusati PC, Ricci CA (eds), Guide book to the excursion on the Paleozoic basement of Sardinia: Siena, IGCP project N.5, Newsletter special issue, pp 31–49

Carmignani L, Carosi R, Di Pisa A, Gattiglio M, Musumeci G, Oggiano G, Pertusati PC (1994) The Hercynian chain in Sardinia (Italy). Geodin Acta 7(1):31–47

Carmignani L, Oggiano G, Barca S, Conti P, Salvadori I, Eltrudis A, Funedda A, Pasci S (2001) Geologia della Sardegna. Note illustrative della Carta Geologica della Sardegna a scala 1:200.000. Memorie descrittive della Carta Geologica d'Italia 60, p 283

Carosi R, Gattiglio M, Musumeci G, Oggiano G (1992) Geologia della catena ercinica in Sardegna - Zona a falde. In: Pertusati PC, Barca S, Carosi R, Di Pisa A, Gattiglio M, Musumeci G, Oggiano G (eds) Carmignani L. Struttura della catena ercinica in Sardegna. Guida all' escursione. Gruppo Informale di Geologia Strutturale, Siena, pp 77–145

Casas JM (2010) Ordovician deformations in the Pyrenees: new insights into the significance of pre-Variscan ("sardic") tectonics. Geol Mag 147(5):674–689

Cathelineau M (1988) Cation site occupancy in chlorites and illites as a function of temperature. Clay Miner 23:471–485

Cathelineau M, Nieva D (1985) A chlorite solid solution geothermometer. The Los Azufrez (Mexico) geothermal system. Contrib Minerals Petrol 91:235–244

Connolly JAD (1990) Multivariable phase diagrams; an algorithm based on generalized thermodynamics. Am J Sci 290:666–718

Corradini C, Barca S, Spalletta C (2003) Late Devonian-Early Carboniferous conodonts from the "Clymeniae Limestones" of SE Sardinia (Italy). Courier Forschungs-Institut Senckenberg 245:227–253

Correia Romão JM, Coke C, Dias R, Ribeiro A (2005) Transient inversion during the opening stage of the Wilson cycle "Sardic phase" in the Iberian Variscides – Stratigraphic and tectonic record. Geodin Acta 18:115–129

Cruciani G, Franceschelli M, Caredda AM, Carcangiu G (2001) Anatexis in the Hercynian basement of NE Sardinia, Italy: a case study of the migmatite of Porto Ottiolu. Mineral Petrol 71:195–223

Cruciani G, Franceschelli M, Groppo C, Spano ME (2012) Metamorphic evolution of non-equilibrated granulitized eclogite from Punta de li Tulchi (Variscan Sardinia) determined through texturally controlled thermodynamic modeling. J Metamorph Geol 30:667–685

Cruciani G, Fancello D, Franceschelli M, Scodina M, Spano ME (2014a) Geothermobarometry of Al-silicate-bearing migmatites from the Variscan chain of NE Sardinia, Italy: a P-T pseudosection approach. Per Mineral 83(1):19–40

Cruciani G, Franceschelli M, Foley SF, Jacob DE (2014b) Anatectic amphibole and restitic garnet in Variscan migmatite from NE Sardinia, Italy: insights into partial melting from mineral trace elements. Eur J Mineral 26:381–395

Cruciani G, Franceschelli M, Battaglia S, Pasci S, Puxeddu M (2015a) Zn-Al-rich chlorite in interleaved phyllosilicate grains from the low-temperature metamorphic Ordovician terrane of Iglesiente, south-west Sardinia, Italy. Mineral Petrol 109:713–718

Cruciani G, Franceschelli M, Groppo C, Oggiano G, Spano ME (2015b) Re-equilibration history and P-T path of eclogites from Variscan Sardinia, Italy: a case study from the medium-grade metamorphic complex. Int J Earth Sci 104:797–814

Del Bono GL (1965) Relazione generale su una possibile interpretazione sulla serie cambrico-ordoviciana dell'Iglesiente. Resoconti dell'Associazione Mineraria Sarda 70:5–134

Dunnet D (1969) Deformation in Paleozoic rocks of Iglesiente, SW Sardinia: PhD thesis, University of London, p 412

Fettes D, Desmons J (2007) Metamorphic Rocks—A Classification and Glossary of Terms. Cambridge University Press, p 244

Franceschelli M, Memmi I, Ricci CA (1982) Ca distribution between almandine-rich garnet and plagioclase in pelitic and psammitic schists from the metamorphic basement of north-eastern Sardinia. Contrib Mineral Petrol 80:285–295

Franceschelli M, Mellini M, Memmi I, Ricci CA (1989) Sudoite, a rocks-forming mineral in Verrucano of the Northern Apennines (Italy) and the sudoite-chloritoid- pyrophyllite assemblages in prograde metamorphism. Contrib Mineral Petrol 101:274–279

Franceschelli M, Memmi I, Gianelli G (1991) Re-equilibration of detrital muscovite and the formation of interleaved phyllosilicate grains in low-temperature metamorphism, northern Apennines, Italy. Contrib Mineral Petrol 109:151–158

Franceschelli M, Puxeddu M, Memmi I (1998) Li, B-rich Rhaetian metabauxite, Italy: reworking of older bauxite and igneous rocks. Chem Geol 144:221–242

Franceschelli M, Carcangiu G, Caredda AM, Cruciani G, Memmi I, Zucca M (2002) Transformation of cumulate mafic rocks to granulite and re-equilibration in amphibolite and greenschist facies in NE Sardinia, Italy. Lithos 63:1–18

Franzini M, Leoni L, Saitta M (1975) Revisione di una metodologia analitica per fluorescenza X basata sulla correzione completa degli effetti di matrice. Rend Soc Ital Miner Petrol 31:365–378

Frey M (1969) A mixed-layer paragonite/phengite of low-grade metamorphic origin. Contrib Mineral Petrol 24:63–65

Gaggero L, Oggiano G, Funedda A, Buzzi L (2012) Rifting and arc-related Early Paleozoic volcanism along the North Gondwana

margin: geochemical and geological evidence from Sardinia (Italy). J Geol 120:273–292

Hillier S, Velde B (1991) Octahedral occupancy and chemical composition of diagenetic (low-temperature) chlorites. Clay Miner 26:149–168

Holland TJB, Powell R (1998) An internally consistent thermodynamic data set for phases of petrological interest. J Metamorph Geol 16:309–343

Holland TJB, Baker JM, Powell R (1998) Mixing properties and activity-composition relationships of chlorites in the system MgO-FeO-Al_2O_3-SiO_2-H_2O. Eur J Mineral 10:395–406

Krumm S (1996) An interactive Windows program for profile fitting and size/strain analysis. Mater Sci Forum 228–231:183–190

Kübler B (1990) "Cristallinity" de l'illite et mixed-layer: brève révision. Schweiz Mineral Petrogr Mitt 70(1):89–93

Lanari P, Wagner T, Vidal O (2014) A thermodynamic model for di-trioctahedral chlorite from experimental and natural data in the system MgO-FeO-Al_2O_3-SiO_2-H_2O: applications to P-T sections and geothermometry. Contrib Mineral Petrol 167:968

Lefort JP (1989) Basement correlation across the North Atlantic. Springer, Berlin

Leone F, Hamman W, Laske R, Serpagli E, Villas E (1991) Lithostratigraphic units and biostratigraphy of the post-sardic Ordovician sequence in south-west Sardinia. Boll Soc Paleont It 30(2):201–235

Leone F, Loi A, Pillola GL, Storch P (2009) The Late Ordovician (Hirnantian) deposits in the Domusnovas area (SW Sardinia). Rend Soc Paleont It 3(2):227–237

Leoni L (2001) New standardized illite crystallinity data from low - to very-low grade metamorphic rocks (Northern Apennines, Italy). Eur J Mineral 13(6):1109–1118

Linnemann U, Romer RL (2002) The Cadomian Orogeny in Saxo-Thuriniga, Germany: geochemical and Nd–Sr–Pb isotopic characterization of marginal basins with constraints to geotectonic setting and provenance. Tectonophysics 352:33–64

Lo Pò D, Braga R (2014) Influence of ferric iron on phase equilibria in greenschist facies assemblages: the hematite-rich metasedimentary rocks from the Monti Pisani (Northern Apennines). J Metam Geol 32:371–387

Lüneburg CM, Lebit HDW (1998) The development of a single cleavage in an area of repeated folding. J Struct Geol 20:1531–1548

Martini P, Tongiorgi M, Oggiano G, Cocozza T (1991) Alluvial fan to marine shelf transition in SW Sardinia, western Mediterranenan Sea: tectonically (« Sardic Phase ») influenced by clastic Ordovician sedimentation. Sed Geol 72:97–115

Massonne H-J, Willner AP (2008) Phase relations and dehydration behaviour of psammopelite and mid-ocean ridge basalt at very-low-grade to low-grade metamorphic conditions. Eur J Mineral 20:867–879

Massonne H-J, Cruciani G, Franceschelli M (2013) Geothermobarometry on anatectic melts—a high-pressure Variscan migmatite from northeast Sardinia. Int Geol Rev 55:1490–1505

Oggiano G, Gaggero L, Funedda A, Buzzi L, Tiepolo M (2010) Multiple early Paleozoic volcanic events at the northern Gondwana margin: U-Pb age evidence from the Southern Variscan branch (Sardinia, Italy). Gondwana Res 17:44–58

Pasci S, Pertusati PC, Salvadori A, Medda F, Murtas A, Rizzo R, Uras V (in press). Note illustrative della Carta geologica d'Italia 1:50.000 "Foglio 555 Iglesias": Roma, Servizio Geologico d'Italia

Pillola GL (1991) Occurrence of Proteuloma (Trilobita) in the Cabitza Formation (Cambro-Tremadoc, SW Sardinia, Italy): paleobiogeographic implications. Geologia del Basamento italiano, Abstracts, Siena 21-22 marzo 1991, 59–61

Pillola GL, Gross U (1982) Stratigrafia del Membro di Matoppa della Formazione di Nebida (Cambrico inferiore) nell'area M.te S. Giovanni-M.te Uda. In: Guida alla Geologia del Paleozoico Sardo, Carmignani L, Cocozza T, Ghezzo C, Pertusati PC, Ricci CA (eds) Roma, Soc Geol It. Guide Geologiche Regionali, p 79–82

Pillola GL, Leone F, Loi A (1995) The Lower Cambrian Nebida Group of Sardinia. Rend Sem Fac Sci Univ Cagliari, suppl. vol. LXV, 27–62

Pillola GL, Piras S, Serpagli E (2008) Upper-Tremadoc-Lower Arenig? Anisograptid-Dichograptid fauna from the Cabitza Formation (Lower Ordovician, SW Sardinia, Italy). Revue de Micropaleontologie 51:167–181

Pittau P, Del Rio M, Funedda A (2008) Relationships between plant communities characterization and basin formation in the Carboniferous-Permian of Sardinia. Boll Soc Geol It 127(3):18–36

Poll JJK (1966) The geology of the Rosas-Terreseo area, Sulcis, South Sardinia. Leidse Geol Meded 35:117–208

Poll JJK, Zwart HJ (1964) On the tectonics of the Sulcis area. S Sardinia: Geol en Mijnbouw 43:144–146

Rossi P, Oggiano G, Cocherie A (2009) A restored section of the "southern Variscan realm" across the Corsica-Sardinia microcontinent. CR Geosci 341:224–238

Ruiz Cruz MD, Sanz de Galdeano C (2005) Compositional and structural variation of sudoite from the Betic Cordillera (Spain): a TEM/AEM study. Clay Clay Minerals 53(6):639–652

Sassi FP, Scolari A (1974) The b_0 value of the potassic white mica as a barometric indicator in low-grade metamorphism of pelitic schist. Contrib Mineral Petrol 45:143–152

Stille H (1939) Bemerkungen betreffend die "Sardische" Faltung und den Ausdruck "ophiolithisch". Z Deut Geol Ges 91:771–773

Teichmüller R (1931) Zur Geologie des Thyrrhenisgebietes. Teil 1: Alte und junge Krustenbewegungen im südlichen Sardinien. Abhandlungen von der Gesellschaft der Wissenschaften zu Göttingen, Mathematisch-Physikalische Klasse 3:857–950

Viti C (2011) Exploring fault rocks at the nanoscale. J Struct Geol 33:1715–1727

von Raumer JF, Bussy F, Schaltegger U, Schulz B, Stampfli GM (2013) Pre-Mesozoic Alpine basements- Their place in the European Paleozoic framework. Geol Soc Am Bull 125:89–108

Wimmenauer W (1984) Das praevariszische Kristallin im Schwarzwald. Fortschritte der Mineralogie: Beiheft 62:69–86

Zane A, Weiss Z (1998) A procedure for classifying rock-forming chlorites based on microprobe data. Rend Lincei Sci Fisiche e Nat 9:51–56